Hydrology Drives Crustal Deformation and Modulates Seismicity in the Matese Massif (Italy)

Francesco Pintori*[1], Federica Sparacino[2], and Federica Riguzzi[3]

Abstract

We analyze the interplay between hydrology, deformation, and seismicity in the Matese massif, located in the Italian Southern Apennines. We find that this area is characterized by the concurrent action of two hydrologically driven processes: the first is the deformation detected by the Global Navigation Satellite Systems (GNSS) data in the shallowest part (above the elevation of the major springs) of the Earth crust, in phase with the hydrological forcing; the second is the triggering of seismicity at depth with a delay suggesting a downward diffusive process. We study the first process by applying a principal component analysis to the GNSS displacements time series, aiming to identify a common signal describing the largest data variance. We find that the maximum horizontal displacements associated with the first principal component (PC1) are larger than 1 cm in two GNSS sites, and the PC1 temporal evolution is well correlated and in phase with the flow of the largest spring of the region, which we consider as proxy of the water content of the massif. This suggests that the main source of horizontal deformation is the water content fluctuations in the shallow portion of the Matese aquifer, in particular within fractures located in correspondence of the main mapped faults. The deformation rates caused by this process are one order of magnitude larger than the tectonic ones. Finally, we infer the second process by observing the correlation between the background seismicity and the spring discharge with a time lag of 121 days. In our interpretation, downward diffusive processes, driven by aquifer water content variations, propagate pore-pressure waves that affect the fault's strength favoring the occurrence of microearthquakes. This is supported by the values of hydraulic diffusivity (1.5 m^2/s) and rock permeability (3.2–3.8 × 10^{-13} m^2), which are compatible with what is observed in karstified limestones.

Cite this article as Pintori, F., F. Sparacino, and F. Riguzzi (2023). Hydrology Drives Crustal Deformation and Modulates Seismicity in the Matese Massif (Italy), *Seismol. Res. Lett.* **XX**, 1–14, doi: 10.1785/0220230239.

Supplemental Material

Introduction

The space geodetic measurements available in Europe in the last 20 yr, in particular the Global Navigation Satellite Systems (GNSS), have shown that hydrological processes play an important role in driving both horizontal and vertical crustal deformations. Silverii *et al.* (2019) showed that the Italian Apennines are characterized by heterogeneous horizontal displacement patterns, which are related to variations of the water content within the aquifers. The proposed source of deformation for the horizontal displacement, in mountainous context, is the water level variation within the aquifer hosted by the mountains. Such fluctuations, especially in karst aquifers, can be very large, causing stress variations responsible for both anisotropic deformation and seismicity modulation, as shown by Pintori *et al.* (2021), D'Agostino *et al.* (2018), and Devoti *et al.* (2018).

As recently discussed by Hsu *et al.* (2021), the natural water cycle can modulate the seismicity in different ways: the crustal load associated with wet periods, for which the water content increases, is potentially able to induce a direct stress variation on the fault plane. For example, Bollinger *et al.* (2007) observed a seismicity rate decrease in the Himalaya of Nepal in summer months and interpreted it as caused by water loading increase occurring during the summer monsoon. In fact, an increase of elastic stress generated by this process induces a normal stress increase in the fault planes, which reduces the Coulomb failure conditions and partially inhibits the seismicity, whereas the shear stress on fault planes can both increase and reduce

1. Istituto Nazionale di Geofisica e Vulcanologia, Sezione di Bologna, Bologna, Italy, https://orcid.org/0000-0001-7465-6297 (FP); 2. Istituto Nazionale di Geofisica e Vulcanologia, Osservatorio Etneo, Catania, Italy, https://orcid.org/0000-0002-7851-9545 (FS); 3. Istituto Nazionale di Geofisica e Vulcanologia, Osservatorio Nazionale Terremoti, Rome, Italy

*Corresponding author: francesco.pintori@ingv.it

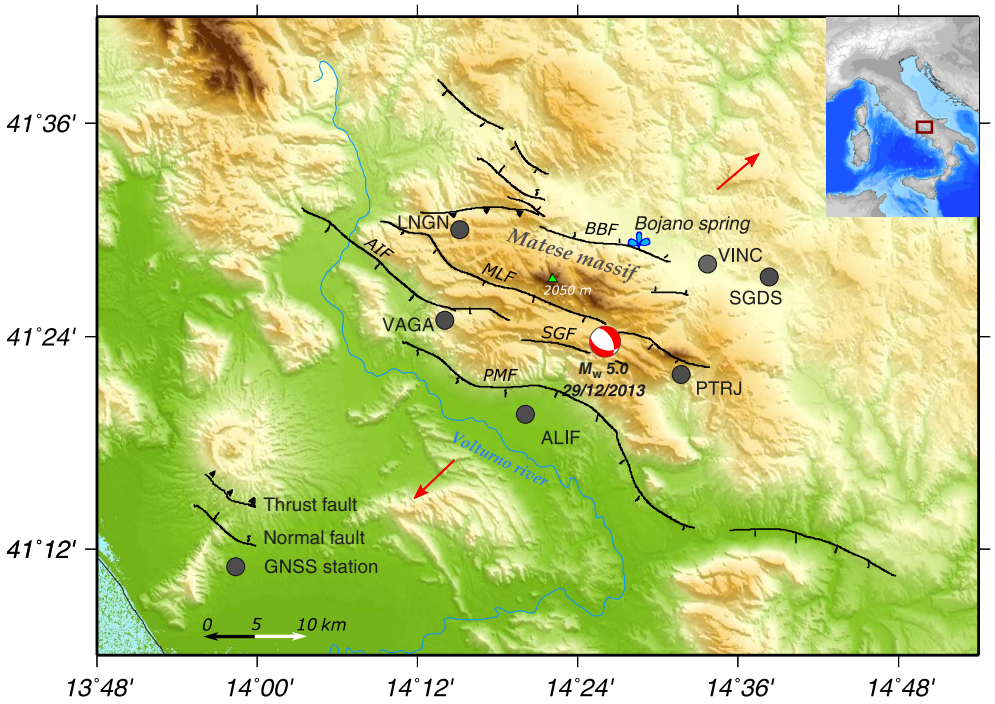

Figure 1. The study area and its location with respect to the Italian peninsula (inset). The black lines represent the main faults (Esposito *et al.*, 2020; Boncio *et al.*, 2022): Aquae Iuliae fault (AIF), Bojano Basin fault (BBF), Matese Lake fault (MLF), Piedimonte Matese fault (PMF), and San Gregorio fault (SGF). The focal mechanism of the 29 December 2013 M_w 5.0 (red and white focal mechanism plot) is normal (see Data and Resources) and in agreement with the extensional tectonic style of the area (red arrows; Serpelloni *et al.*, 2022). Symbols for Global Navigation Satellite Systems (GNSS) stations (black dots) and spring (sky blue clover) are indicated on the map. The color version of this figure is available only in the electronic edition.

the Coulomb failure conditions, depending on the fault mechanism (i.e., the rake and dip angles; Roeloffs, 1988). Another example of the direct hydrological-induced stress on fault planes is from Craig *et al.* (2017), who showed that the microseismic activity in the New Madrid seismic zone (central United States) is modulated by the continental water storage variations at both annual and multi-annual timescales, with no significant time lag.

On the other hand, the water accumulation on the surface generates pore pressure variations, which propagate downward and can reach hypocentral depth increasing the Coulomb failure conditions by reducing the effective friction coefficient, favoring the occurrence of seismic events (Roeloffs, 1988).

The direct stress variations caused by the increasing or decreasing water load and pore pressure variations are two processes influencing the faults' stress conditions (Rice and Cleary, 1976) that can be distinguished by analyzing the time lag between the hydrological forcing and the seismicity rates. In fact, the first has an instantaneous effect on the fault plane, so that no lag between the hydrological and seismological signals is recorded; whereas pore pressure variations need time to propagate, then a time lag is recorded (Talwani, 1997).

One of the first examples of natural hydrological processes modulating the seismicity rates was observed by Hainzl *et al.* (2006), who proposed the pore pressure variations induced by rainfall events as driver of the shallow earthquakes occurring in Mt. Hochstaufen (European Alps). More recently, Johnson *et al.* (2020) found that in Alaska the seismicity rates were correlated, with a 3 months lag, with the annual hydrological cycle and interpreted this lag as the time needed by the pore pressure variation to reach seismogenic depths; whereas Montgomery-Brown *et al.* (2019) showed that in the mountains near Long Valley Caldera (California), considering 3–4 weeks of lag, the shallow (<4 km) seismicity rates were strongly influenced by groundwater level variations, which mainly depend on snowmelt.

According to Schuite *et al.* (2017), the propagation time of the pore pressure variation is L^2/D, in which L is the distance that the pore pressure variations have to cover, whereas D is the media or fracture diffusivity.

Here, we study the deformations and the background seismicity of the Matese massif, an extensive outcrop of Apenninic Platform carbonate rocks located at the boundary between Central and Southern Apennines, extending ~74 km from northwest to southeast over an area of ~1600 km^2 and reaching a maximum height of 2050 m (Monte Miletto). The massif primarily consists of sedimentary rocks formed during the Mesozoic that were folded and thrusted during the Cenozoic, causing intense faulting and uplift in the region. Then, during the late Miocene, extensional tectonics took place. The present structure of the massif originates from the Quaternary motion on northwest–southeast-striking extensional faults overlapped to earlier thrust and transpressional deformation (Patacca and Scandone, 2007; Ferrarini *et al.*, 2017; and references therein). The Matese massif is characterized by several faults generally northwest–southeast directed (Fig. 1): the northeast-dipping Bojano basin normal fault (BBF, probably responsible for the 1456 and 1805 events); the southwest-dipping normal Aquae Iulie fault

(AIF, recognized as active and possibly associated with the 1349 earthquake), Matese Lake (MLF), San Gregorio (SGF), and Piedimonte Matese faults (PMF; Boncio *et al.*, 2022; Esposito *et al.*, 2020; and reference therein). Furthermore, the present seismotectonic background belongs to the extensional style of the central-southern Apennine chain, which is characterized by 3–4 mm/yr (Devoti *et al.*, 2017) tectonic extension, with a series of northwest–southeast active extensional faults and the occurrence of seismic activity, reaching in the past intensities up to IX Mercalli–Cancani–Sieberg (Rovida *et al.*, 2022).

This area is of particular interest because the Matese undergoes karst processes with significant response to hydrologic processes, linking rainfall trends to large variations of water reservoirs (Fiorillo and Pagnozzi, 2015). The rocks have low primary permeability, but they are extensively fractured so that groundwater mainly flows within a network of interconnected fractures (Celico *et al.*, 2006). The hydrogeologic features of the area, where recent studies (Leone *et al.*, 2023) highlighted a role of the fluids in driving the deformations, and the intense seismic activity makes the Matese massif an interesting area for the study on the interplay among water storage variations, deformation, and seismicity. The articles mentioned earlier describe the hydrological features of this study area, how they drive the deformations of Matese massif. In this work, besides confirming the dominant presence of hydrological processes as sources of deformation, we try to determine the spatiotemporal features of the common displacement pattern and, more importantly, analyze if and how the hydrological processes modulate the seismicity rates.

Because it has been measured that the hydraulic conductivity of the karstified limestone decreases significantly with depth (Celico *et al.*, 2006), we can hypothesize that the Matese deformations are activated mainly by hydrological processes acting in the very shallow portion of the Earth crust, that is, the first few hundreds of meters, where crust fractures open and close during the recharge and discharge phases of the aquifer. On the other hand, we study whether the background seismicity shows any pattern that might be related to hydrological processes and whether it is influenced by direct stress variation on the fault plane or by the faults strength reduction, produced by pore pressure diffusion.

To extract the largest common displacement signal from the GNSS time series, we perform a principal component analysis (PCA, Jolliffe, 2002), one of the most effective and widely used methods employed to identify such a common displacement signal recorded by the GNSS network.

PCA in the GNSS time series analysis allows us to identify the displacement signals that explain the largest variance of the GNSS data set. This is useful to extract from a large data set covering large areas spatially correlated signals, which the geodesists often call common-mode errors, that can result from large scales nontectonic processes or GNSS data processing errors (Dong *et al.*, 2002; Serpelloni *et al.*, 2018). When considering a reduced number of GNSS stations, as the case presented here, the signals extracted by the PCA might be related to seismic events (Gualandi *et al.*, 2014) or to local hydrological processes (Nespoli *et al.*, 2021). Unlike the stacking methods, which identify a common displacement signal that has the same temporal evolution and amplitude at each station; PCA extracts signals with the same temporal evolution, but with variable amplitudes. This allows us to recognize the stations that are affected by the common displacement signal and which is its spatial orientation.

The article is organized as follows: we first describe the data and methods used in this work; then, we show the results of the PCA on both horizontal and vertical displacement components. Finally, we discuss and try to interpret how hydrological processes influence both deformation and seismicity rates.

Data and Methods

In this work, we consider the north, east, and vertical displacement components of six GNSS stations located in the Matese massif and its surroundings (Fig. 1); seismological data from the catalog described by Diaferia *et al.* (2023); daily observations of spring discharge provided by Regione Campania and Regione Molise Technical Services and the German Research Centre for Geosciences (GFZ) products that model the displacements caused by both the hydrological and the nontidal atmospheric loading. The GNSS observations are processed using Bernese software version 5.0 (Beutler *et al.*, 2007) following a standard approach for high precision positioning routinely exploited at the Istituto Nazionale di Geofisica e Vulcanologia (INGV) to analyze more than one thousand stations in the Italian area and European plate (Devoti *et al.*, 2017). The time series consists of daily estimates of station positions, detrended from secular drifts and corrected for offsets due to instrumental changes, without removal of any periodical component that could be relevant for our purposes. GNSS data are then analyzed by applying a PCA on the GNSS time series, with the goal of extracting a common displacement pattern that describes the largest data variance. The PCA works by reducing the dimension of the data, and this allows it to extract common spatiotemporal features from the data set. This is achieved by projecting the data in a new coordinate system where the new axes, called principal components (PCs), are orthogonal, that is, they are uncorrelated. Each PC is characterized by a common temporal evolution and a different spatial response at each measurement site. Because the latest study on the Matese massif deformation (Leone *et al.*, 2023) has shown that the vertical and horizontal components of the displacement are quite different, we decided to apply a PCA on the vertical and horizontal components of the displacement

separately, adopting the PCA technique described in Gualandi *et al.* (2016), which is incorporated in the PCA-based inversion method software (PCAIM, Kositsky and Avouac 2010), because it has the great advantage of being able to take into account missing data while performing the decomposition of the data matrix.

The seismological data are provided as a detailed catalog of the Matese area, which is a part of a larger catalog encompassing the southern Apennines, obtained after using a template-matching procedure, a cross-correlation based technique for the detection of hidden earthquakes. The catalog contains 2489 events from January 2009 to December 2014 and has been realized to study the seismicity of the area with particular regard to the seismic sequence that started on 29 December 2013 and lasted for several days (Diaferia *et al.*, 2023). During the first day of the seismic sequence, 176 earthquakes were recorded, including the M_w 5.0 mainshock, whereas the number of events detected in 2014 is much larger than in the previous years (Fig. S1, available in the supplemental material to this article). Because here we want to study the rates of the background seismicity, which is affected by the beginning of this relatively large seismic sequence, we limited the seismicity time series from January 2009 to 29 December 2013. Therefore, our seismic data set consists of about 1080 seismic events with most of magnitudes M_L within the range –0.3 to 3.2. We have analyzed this catalog with ZMAP software package (Wiemer, 2001), obtaining a completeness magnitude of M_c 0.6, and finally it was declustered with the Gardner and Knopoff algorithm (Gardner and Knopoff, 1974), which was proved to be the most reliable in the Italian area (Taroni and Akinci, 2021). The resulting data set consists of 764 events. The histograms of the event magnitudes and of the hypocentral depths are provided in Figure S1.

In this work, we estimate the background seismicity rates, in particular their temporal variations, by cumulating the daily number of earthquakes and then removing the linear trend. As a result, a time series representing the excess or lack of seismic events over a constant rate is obtained.

Finally, hydrological and nontidal atmospheric loading are estimated by the land surface discharge model (LSDM, Dill, 2008), which simulates global water storage variations of surface water in rivers, lakes, wetlands, soil moisture, and water stored as snow and ice, but does not account for deep groundwater variations. The LSDM inputs are precipitation, evaporation, and temperature from an atmospheric model developed by the European Centre for Medium-Range Weather Forecasts. Finally, surface displacements caused by the LSDM-based continental hydrology and nontidal atmospheric surface pressure variations are computed using the Green's function approach as in Dill and Dobslaw (2013) with a daily temporal resolution and a spatial resolution of 0.5°.

Analysis of the Displacement Field

PCA on the horizontal components

We perform a PCA on the horizontal components of the GNSS time series, considering the time interval from January 2008 to August 2022. Our goal is to extract a common displacement signal that describes the largest variance of the data set, which is associated with the first principal component (PC1) resulting from this analysis. PC1 explains 67% of the data variance. PC1 temporal evolution (V1, Fig. 2a) is the same for all the stations; it is nondimensional and normalized between 0 and 1. V1 is a sinusoidal annual signal for which the amplitude is variable; the peaks of V1 occur during the spring, and the lows during the fall. The orientation and amplitude of the PC1 displacements, that is, the PC1 spatial distribution (U1, in millimeters), is represented as white arrows in Figure 2b.

The displacement related to the PC1 between two epochs (e.g., $t1$ and $t2$, with $t2 > t1$) at a given station n is calculated as $V1(t2) \times U1n\text{-}V1(t1) \times U1n$, in which $V1(t2)$ is the value associated with the PC1 temporal evolution (Fig. 2a) at the epoch $t2$, whereas $U1n$ is characterized by two values indicating the amplitude of the spatial response of station n in the east and north components. It follows that, during the time interval $t2$–$t1$, if V1 increases ($V1(t2) > V1(t1)$), the station moves in the horizontal plane in the direction indicated by the white arrow. Conversely, if V1 decreases during the interval $t2$–$t1$ ($V1(t2) < V1(t1)$), the station moves in the horizontal plane in the opposite direction to the direction indicated by the white arrow. As an example, LNGN moves northward when V1 is increasing and southward when V1 is decreasing.

The length of the arrows represents the maximum displacements associated with PC1, computed for each station as the difference of the station position between the epochs where V1 is maximum and V1 is minimum. Although the presence of some outliers in the V1 lead to maximum displacements that are a little bit overestimated, in the GNSS station VAGA the maximum displacements associated with this component have a maximum amplitude in the east and north component of about 2 cm and 3 cm, respectively.

Both the great similarity between the V1 temporal evolution and VAGA displacements (Fig. 3) and the amplitude of the PC1 spatial response in VAGA, which is much larger than the ones associated with the other five stations, might suggest that the PC1 is only driven by some very local signals that only involve VAGA. To test whether the deformation signal associated with PC1 only involves VAGA or it is actually present also in the remaining GNSS sites, we perform another PCA excluding VAGA from the data set. To distinguish between these two PCA analyses, we next call the PCA analysis including VAGA "PCA_VAGA" and "PCA_noVAGA" for the analysis performed excluding VAGA.

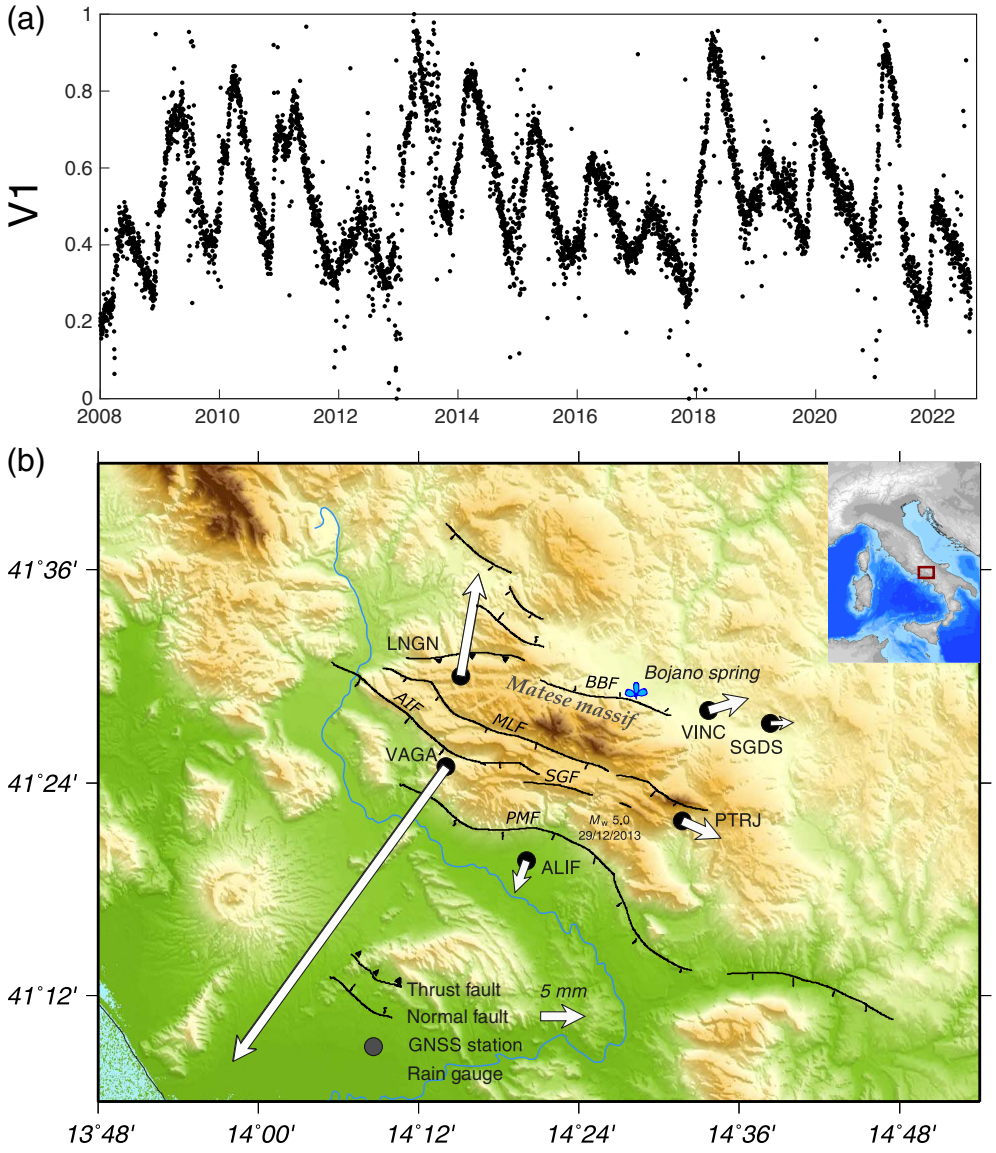

Figure 2. (a) Temporal evolution (V1), normalized between 0 and 1 and (b) spatial distribution of PC1_VAGA. Each white arrow represents the maximum displacement, associated with the principal component, reached by each GNSS site. The inset represents the study area and its location with respect to the Italian peninsula. The color version of this figure is available only in the electronic edition.

The PC1_noVAGA temporal evolution (V1_noVAGA) is more scattered than V1_VAGA, but after filtering V1_noVAGA with a 15-days moving average filter V1_noVAGA appears quite similar to V1_VAGA (Fig. 5).

Both including and not including VAGA in the PCA, we obtain as PC1 a component characterized by a sinusoidal temporal evolution with an annual periodicity, for which the amplitude is not constant.

The comparison between PCA_noVAGA and PCA_VAGA shows that VAGA has a large influence on driving the PC1 features but also that an annual displacement signal, with variable amplitude, is not only locally present in VAGA. In fact, PC1_noVAGA shows that this horizontal deformation signal affects all the GNSS stations located in the study area with maximum amplitudes up to several millimeters.

PCA on the vertical component

We perform a PCA on the vertical component of the GNSS time series, assuming that the vertical deformation signals are not strictly linked to the horizontal ones. Figure 6a represents PC1 temporal evolution (V1), whereas Figure 6b shows PC1 spatial distribution (U1), for which the color of the dots represents the maximum vertical displacements associated with PC1. Here, the displacements are computed as described in the PCA on the horizontal components section, with the difference that in this case the U1 at a station *n* is defined by a single component, and then U1 is represented as colored dots instead of arrows. The spatial distribution is quite coherent, positive in all the six GNSS stations, meaning that when the temporal evolution is increasing the GNSS stations are moving upward, whereas when V1 is decreasing the stations are moving downward. The temporal evolution is characterized by a very high frequency; there is not any clear periodicity, and it is very different from the

The PC1_noVAGA explains 36% of the data variance, which is smaller than the variance explained by PC1_VAGA. This is probably due to the large VAGA displacements, which, on the one hand, absorb a significant part of the variance in the data and, on the other hand, are very well reconstructed by PC1 (Fig. 3a). PC1_noVAGA shows a similar spatial distribution in terms of orientation of the displacements, whereas the amplitudes, except for the station LNGN, are larger than the ones obtained with PCA_VAGA (Fig. 4). This is likely a consequence of the fact that the actual displacements in the GNSS stations ALIF, VINC, SGDS, and PTRJ are better reproduced by PC1_noVAGA than PC1_VAGA, as shown in Figures S2 and S3.

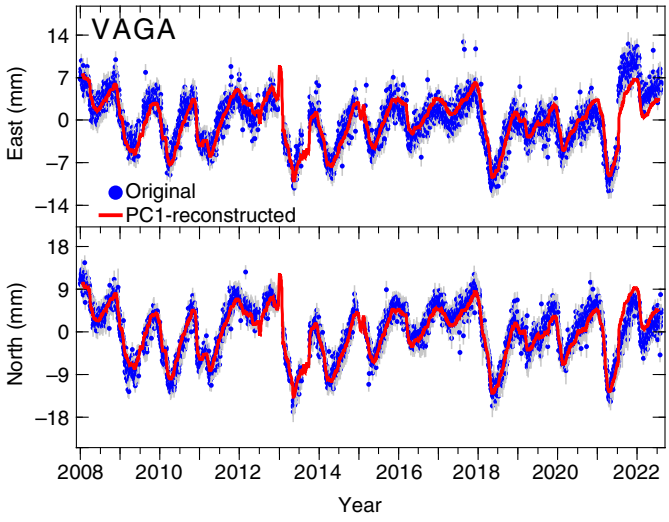

Figure 3. Comparison between the original (blue dots) and principal component analysis (PCA)-reconstructed horizontal displacement components of VAGA. A Gaussian filter is applied on the time series to reduce the scattering and better visualize the data. The color version of this figure is available only in the electronic edition.

temporal evolution resulting from the PCA performed on the horizontal component. In this case, PC1 explains 41% of the data variance.

Interactions among Hydrology, Deformation, and Seismicity

Comparison between deformation and hydrology

Let us now consider the PCA_VAGA results, with the goal of identifying the source of deformation causing the displacements associated with PC1. Because previous studies highlighted deformation associated with hydrological processes in this area, we compare the temporal evolution, V1, of the common horizontal displacement signal extracted using the PCA, with the discharge of the Boiano spring, which is the most productive spring of the region, and it is characterized by the most complete discharge time series among the available springs. We assume that the spring discharge is a proxy of the groundwater level: when the groundwater level rises, the spring discharge increases and vice versa, following an approach already adopted by Montgomery-Brown *et al.* (2019) and Silverii *et al.* (2016). Figure 7 shows that the two time series are well correlated without any significant time lag. This suggests that the main driver of the deformation signal associated with PC1 is related to the hydrological features of the area, as already observed by Leone *et al.* (2023). In particular, when the spring discharge is increasing, that is, the groundwater level is rising, the GNSS stations move away from the center of the Matese massif. Furthermore, the direction of the horizontal displacement in the two GNSS sites where the amplitude is the largest, VAGA and LNGN, is oriented perpendicular to the orientation of the faults (Fig. 2). This behavior is in agreement with the deformation patterns already observed in karstified areas of both the Apennines (Silverii *et al.*, 2016; D'Agostino *et al.*, 2018) and the Italian Alps (Devoti *et al.*, 2015; Pintori *et al.*, 2021), where the displacements are interpreted as caused by groundwater level variations within karst fractures. It is worth noting that the PC1 displacements associated with VAGA and LNGN cause deformation rates one order of magnitude larger than the tectonic ones.

On the other hand, the interpretation of the common displacement signal resulting from the analysis of the vertical component of the displacement is less straightforward. Generally, the common displacement signals in the vertical direction are interpreted as common mode errors, resulting from processing errors such as mismodeling of the satellite orbits and/or common mode signals, which are signals caused by an actual source of deformation acting quite uniformly at large scale as the atmospheric pressure variation, the hydrological loading, and the ocean loading (Pintori *et al.*, 2022, and references therein). The high frequency of V1 suggests that atmospheric pressure is a possible forcing for this source of deformation. Then, we computed the daily mean vertical displacement caused by the effect of the hydrological and of the nontidal atmospheric loading.

We averaged the results over a region including the study area with limits longitude: 13.25°–15.25°; latitude: 40.75°–41.25° and compared them with the V1 obtained analyzing the vertical component of the GNSS displacement. We did not find any correlation between PC1 temporal evolution and atmospheric loading. We also tested the combined effect of hydrological and atmospheric loading, but we could not find a correlation between the temporal evolution of the displacement caused by these environmental processes and V1 (Fig. S4a,b).

The comparison between V1 and loading-induced displacements was also performed smoothing the time series with a 30-days moving average filter. Although the smoothing highlights the presence of an annual periodicity in V1, a correlation with the displacements caused by the atmospheric loading or the combined effect of hydrological and atmospheric loading does not emerge (Fig. S4c,d).

It is then likely that this signal is a common mode error associated with the vertical component of the displacement, for which amplitude is large enough to mask other geophysical signals.

Interplay between Hydrology and Seismicity

We compare the seismicity rates with the temporal evolution of the Boiano spring discharge (Fig. 8). As mentioned before, we estimate the excess or deficit of the seismicity compared to a mean seismicity rate computed over the investigated time

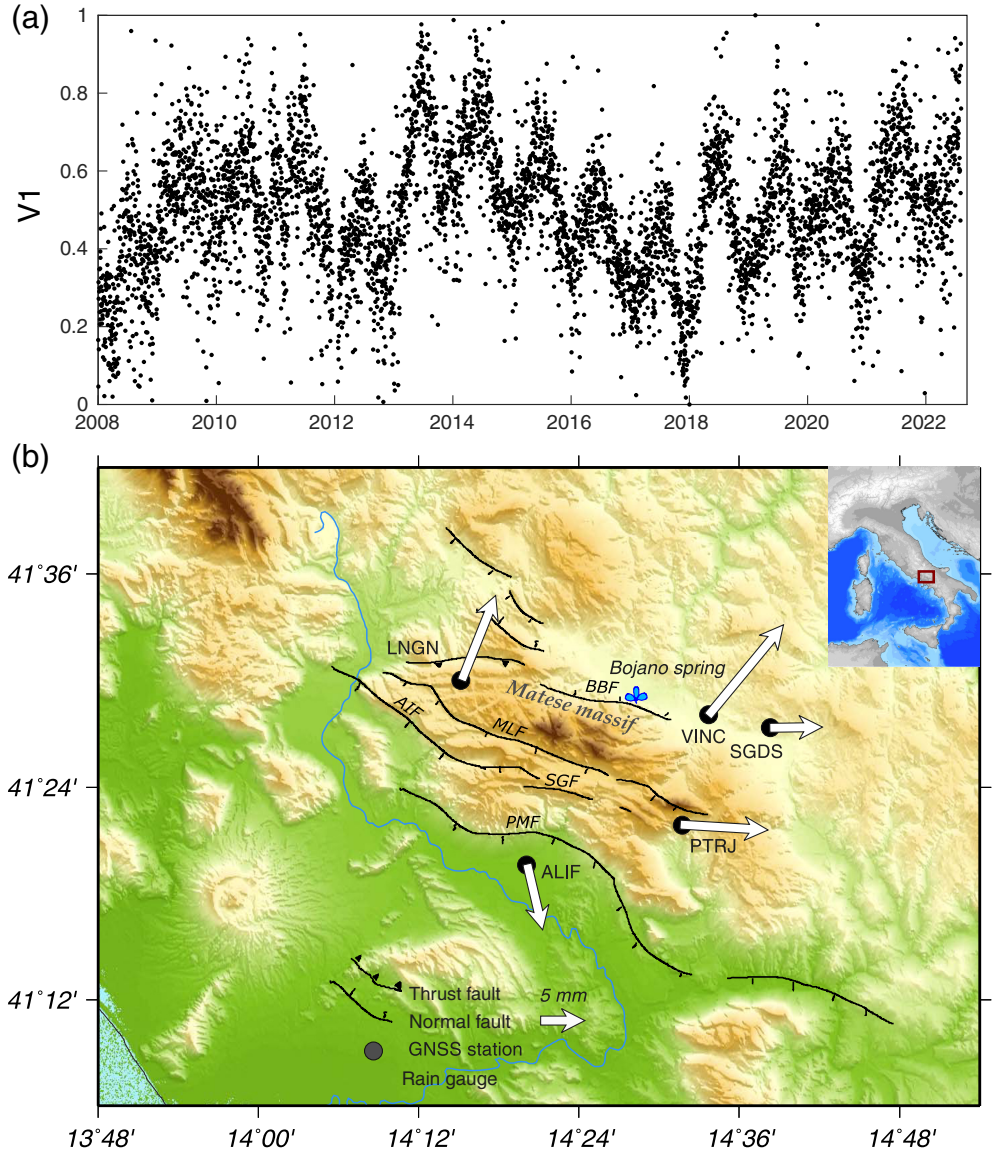

Figure 4. (a) Temporal evolution and (b) spatial distribution of PC1_noVAGA. The inset represents the study area and its location with respect to the Italian peninsula. The color version of this figure is available only in the electronic edition.

interval. The temporal evolution of the seismicity is characterized by an annual periodicity, as the spring discharge, with the seismicity being delayed compared to the discharge by about 4 months (121 days).

Shifting back the seismicity to maximize the cross correlation, we observe a good correlation. In particular, the 2009.5 and 2013.5 discharge peaks are associated with the maximum excess of the seismicity over the investigated time interval.

The correlation between the spring discharge and seismicity rates, with a delay of a couple of months, was also observed by D'Agostino *et al.* (2018) in the Irpinia sector of the Southern Apennines, which is located a few tens of kilometers south of our study region. It is interesting to observe that, although different fault systems and karst aquifers are involved, the deformation, seismicity, and spring discharge patterns are quite similar to what we observe in the Matese. Here, we observe a larger delay between the discharge and the seismicity rates, but this can be attributed to a deeper hypocenter position of the Matese events (Fig. S1c). In fact, the delay between the hydrological forcing and the seismicity is explained as the time needed for the pore pressure variations to reach the hypocentral depths, where it affects the strength of the faults, modulating the seismicity.

Deformation modeling

It has been recognized that faults play a role in the hydrologic circulation within the Matese karstic massif (Petrella *et al.*, 2015). In fact, the aquifer system looks like a series of interconnected basins, for which boundaries are determined by faults that act as aquitards. In some cases, along these faults, the groundwater table reaches the ground surface increasing the pressure within the fault cores and causing the activation of seasonal springs. The piezometric level variations within a fault core were measured in a limited sector of the massif during the 2003–2006 time interval, and the recorded water level time series showed a significant annual signature with amplitude variations reaching up to 30 m (Celico *et al.*, 2006). Therefore, it is reasonable to assume that the water motion within the structural discontinuities of the karstic limestone is able to induce anisotropic deformation driven by the main direction of structural fractures. Hypothesizing an ideal source of such deformation as an equivalent vertical fracture extending from the surface to a depth d and opening W, it is possible to infer the fracture opening by applying the formula by Gudmundsson (1999), which states that $dW = dP \times 2L(1 - \nu^2)/E$, in which ν and E are the Poisson and Young moduli ($\nu = 0.25$ and $E = 20$ GPa can be chosen as the average value for a fractured limestone, Madhubabu *et al.*, 2016). We assume an average fracture

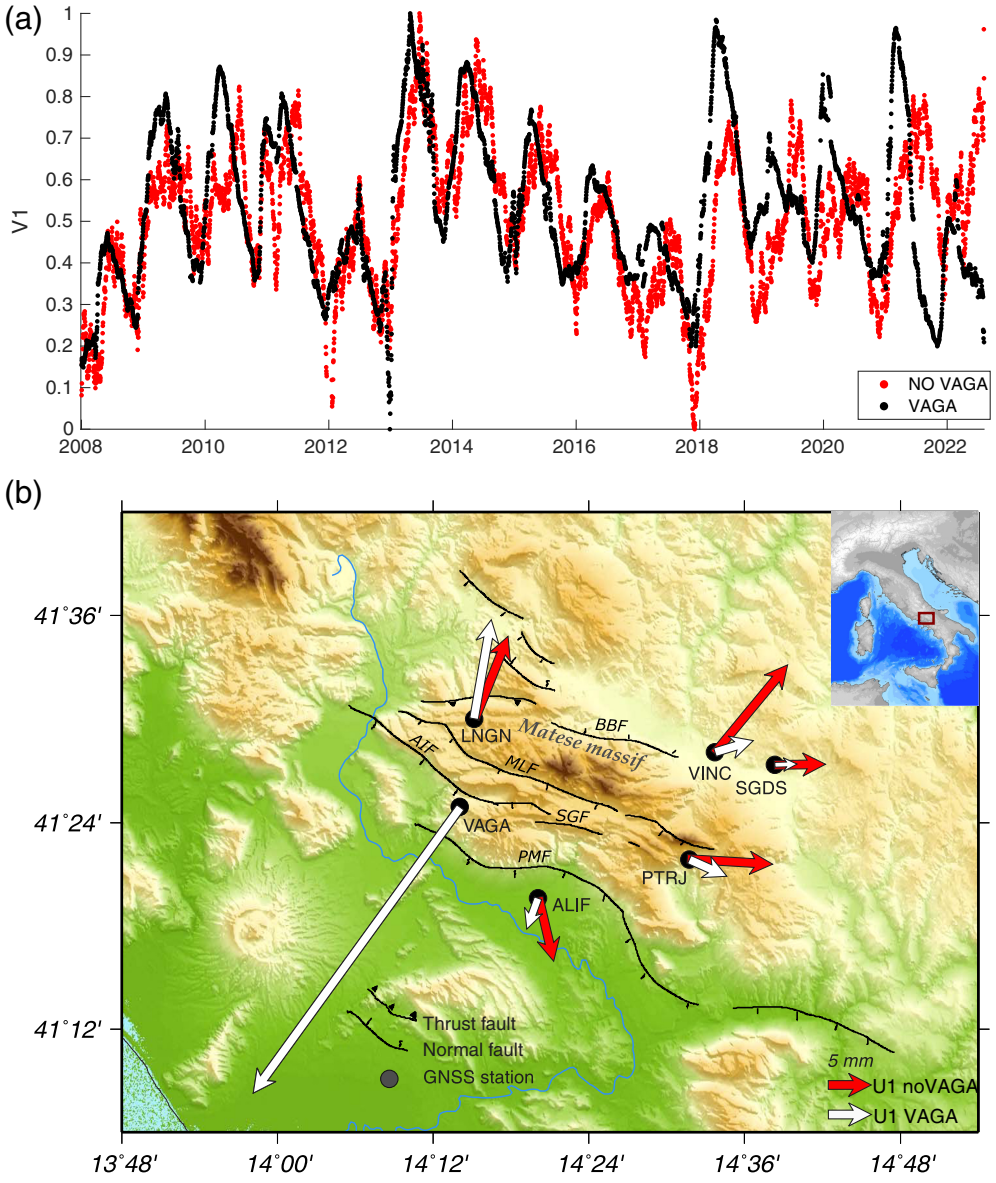

Figure 5. (a) Comparison between V1_noVAGA (red) and V1_VAGA (black). A 15 days moving average filter is applied to both time series. (b) Comparison between the spatial distribution (U1) of the noVAGA (red arrows) and of the VAGA (white arrows) cases. The inset represents the study area and its location with respect to the Italian peninsula. The color version of this figure is available only in the electronic edition.

length L of 3 km because it corresponds to the average rupture length due to a magnitude 5 earthquake (Wells and Coppersmith, 1994), which is the maximum recorded magnitude in the last 50 yr (see Data and Resources). The differential hydrostatic pressure due to water level variation is $dP = \rho \times g \times h$, in which ρ is the water density, g is the gravity acceleration, and h = 30 m, the estimated water level variation according to past piezometric measurements described in Celico *et al.* (2006). In our case $dP \sim 0.3$ MPa, so that the opening variation dW results about 8 cm, in line with what we observed from GNSS common signature.

To test whether the value of dW is reasonable, we build a model to compute the displacement field generated by such a fracture opening, checking whether the modeled results are in agreement with the displacements associated with PC1. In particular, we try to reproduce the displacements of the stations VAGA and LNGN because they are the stations where the largest displacements are recorded. Furthermore, the two stations are characterized by a motion in opposite directions, suggesting that the main source of deformation lies between them.

Following the same approach of Devoti *et al.* (2018), we consider as a possible source of deformation a fracture associated with the shallower part of the AIF, opening up to 8 cm when the water level inside it increases.

The model is based on the finite-element method (FEM) and realized using Comsol Multiphysics software: we consider a 2D elastic half-space with Poisson and Young moduli $\nu = 0.25$ and $E = 20$ GPa. To minimize the boundary effects, the half-space is modeled as a large rectangle where the vertical side is 700 km long and the horizontal side 1400 km long. The fracture, which is equidistant from the vertical sides of the rectangle representing the half-space, is modeled as an elastic tensile dislocation reaching the surface from a depth of 1 km, which is an estimate of the altitude difference between the top of the fault and the discharge springs according to a hydrogeological section proposed by Fiorillo and Pagnozzi (2015). The boundary conditions of this model are "free" surface in the upper horizontal side of the rectangle and "roller," that is, the displacement is zero in the direction perpendicular to the boundary, in the remaining three sides.

To model the displacements recorded by the remaining four GNSS stations, a 3D model would be necessary: the

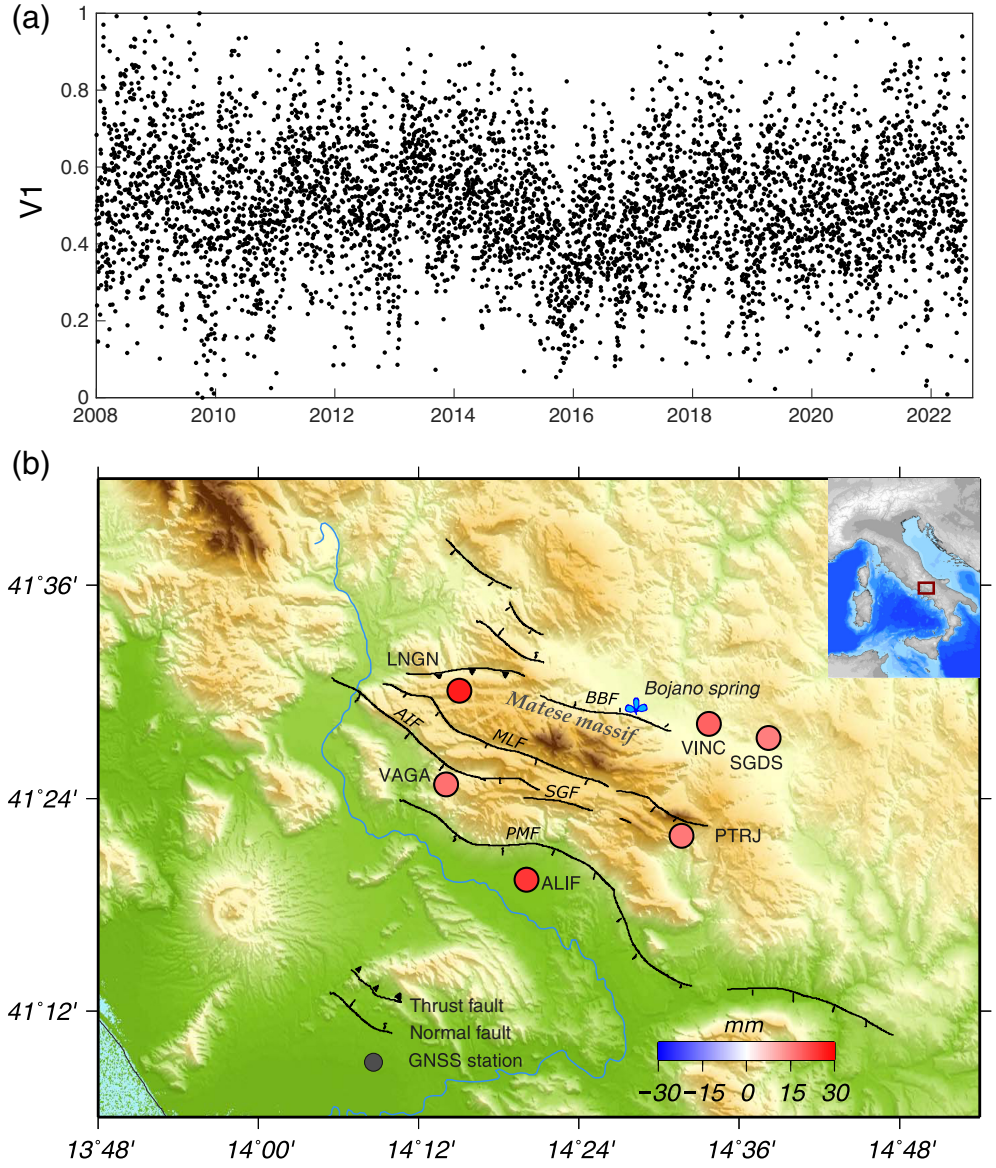

Figure 6. (a) Temporal evolution and (b) spatial distribution of the PC1 performed on the vertical displacements. The inset represents the study area and its location with respect to the Italian peninsula. The color version of this figure is available only in the electronic edition.

orientation of the displacements recorded by the entire GNSS network is not approximately in the same direction because it is considering only LNGN and VAGA. As a consequence, additional potential sources of deformation must be included to model the whole displacement field, but this makes the definition of the model's constraints really difficult and out of the scope of this work.

The FEM model is developed along the profile shown in Figure 9, which is chosen to be perpendicular to the AIF. We compute the horizontal displacement field on the free surface generated by the tensile dislocation, assuming that the walls of the fracture displace 4 cm in opposite directions. The topography is not included in the model because it was shown that in very similar FEM models, as the one presented by Pintori *et al.* (2021), its inclusion does not significantly change the results of the horizontal displacements.

We compare the modeled displacement with the displacements associated with PC1 of LNGN and VAGA, for which both the GNSS station positions and the PC1 displacements are projected along the profile direction. The modeled displacements are a little bit smaller than the ones reconstructed by PC1: 27 mm instead of 40 mm in VAGA and 7 mm instead of 11 mm in LNGN (Fig. 10). Although the model does not perfectly reproduce the observations, it is worth noting that here we considered just one source of deformation, for which parameters are not easy to constrain considering the available information. Therefore, despite the model limitations described earlier, these results still support the thesis that most of the recorded displacements can be explained considering a fracture that opens because of an increase of its water level.

Discussions

Water level fluctuations in fluid reservoirs or aquifer oscillations can affect seismicity rates (e.g., Roeloffs, 1988; Talwani, 1997). Shapiro *et al.* (2003) proposed that the triggering of seismicity and the consequent spatiotemporal evolution can be analyzed in terms of pore pressure relaxation in media with (an)isotropic hydraulic diffusivity. In a poroelastic medium, the extension of the rupture zone can be approximated by the theoretical curve $r = (4\pi \times D \times t)^{1/2}$, in which the distance r of the pressure front from the fluid source (triggering front) is a function of the diffusivity D and time of injection or modulation t. Then, the estimated time lag of 121 days between the aquifer level and seismicity occurrence allows us to infer whether the average value for the pore-pressure diffusivity through the more or less fractured limestone can be realistic.

Considering 14 km as the mean distance between the average depths (Fig. S1) of seismicity and the Bojano spring, and

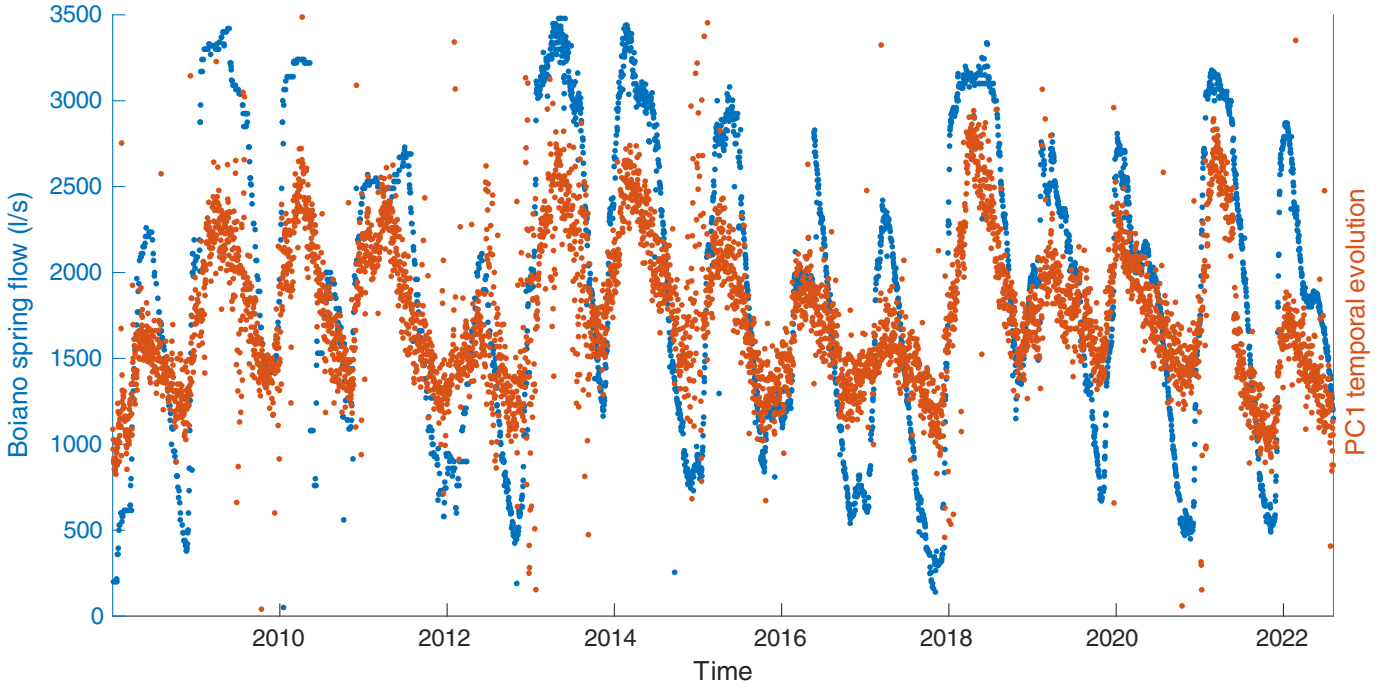

Figure 7. Time series of Bojano spring discharge (blue) and PC1 temporal evolution (orange). The color version of this figure is available only in the electronic edition.

10.5×10^6 s the time lag of the front, we get about $D = 1.5$ m^2/s. From this value, we can also infer the order of magnitude of the rock permeability k. According to Talwani *et al.* (2007), D is proportional to the seismogenic permeability k, $k = D \times \eta \times \Phi \times \beta$, in which η, Φ, and β are the fluid viscosity, the porosity of the rock, and the compressibility of fluid, respectively. In the case of water, $\eta = 10^{-3}$ Pa s, $\beta = 3 \times 10^{-9}$ Pa^{-1} (Di Luccio *et al.*, 2010). Although the product $\eta \times \beta$ remains relatively constant, not only for water, but also for CO_2 rich fluids (Miller *et al.*, 2004), laboratory experiments showed that the limestone porosity Φ may vary in the range 0.06–0.07 (Iscan *et al.*, 2006), so that we obtain a permeability range of about $k = (3.2\text{–}3.8) \times 10^{-13}$ m^2, which should be considered as an order of magnitude estimate. This value is relatively high, but near the lower bound of what is observed in karstified limestone ($10^{-13} < k < 10^{-9}$ m^2) by Sibson and Rowland (2003), and by Di Luccio *et al.* (2010), who studied the pore pressure diffusion in connection with the space–time evolution of aftershocks after the 2009 M_w 6.0 L'Aquila seismic sequence.

We cannot exclude as a possible trigger of seismicity the uprising of deep-seated CO_2 rich fluids, as observed by Di Luccio *et al.* (2010) during the aftershock sequence of the 2009 M_w 6.0 L'Aquila earthquake. However, our case is rather different because the modulation of background seismicity is observed independently from the occurrence of a mainshock and well agree with the observed aquifer and deformation oscillations.

Conclusions

The Matese massif is a region characterized by both quite intense seismic activity and by peculiar deformation patterns, which depend on the hydrogeological features of the area. This makes the Matese a very interesting region for the study of the interplay between hydrological processes, deformation, and seismic activity.

Our results show that the displacements recorded by the GNSS network are correlated and in phase with the spring discharge data, suggesting that the largest variance of the horizontal displacement field is associated with the water level variations in the shallowest part of the Matese aquifer, above the elevation of the major springs. Furthermore, the newly applied PC analysis confirms the recent results of Leone *et al.* (2023) and highlights that the hydrologically induced deformation pattern is likely driven by the fracture orientation.

More interestingly, the new seismic catalog recently provided by Diaferia *et al.* (2023), which contains a significant number of low-magnitude earthquakes never identified before, has allowed us to highlight, for the first time in this region, that the variation of the water content in the Matese aquifer generates downward diffusive processes that induce a modulation of the background seismic activity. In fact, the time lag between the seismicity rates and the hydrological data suggests that the modulation of the seismicity is not primarily caused by any elastic stress variation induced by the aquifer water mass change that generates the observed displacement pattern, but rather by pore pressure variations that need time to propagate until reaching the hypocenter depths, where they reduce the fault's strength. Nonetheless, we

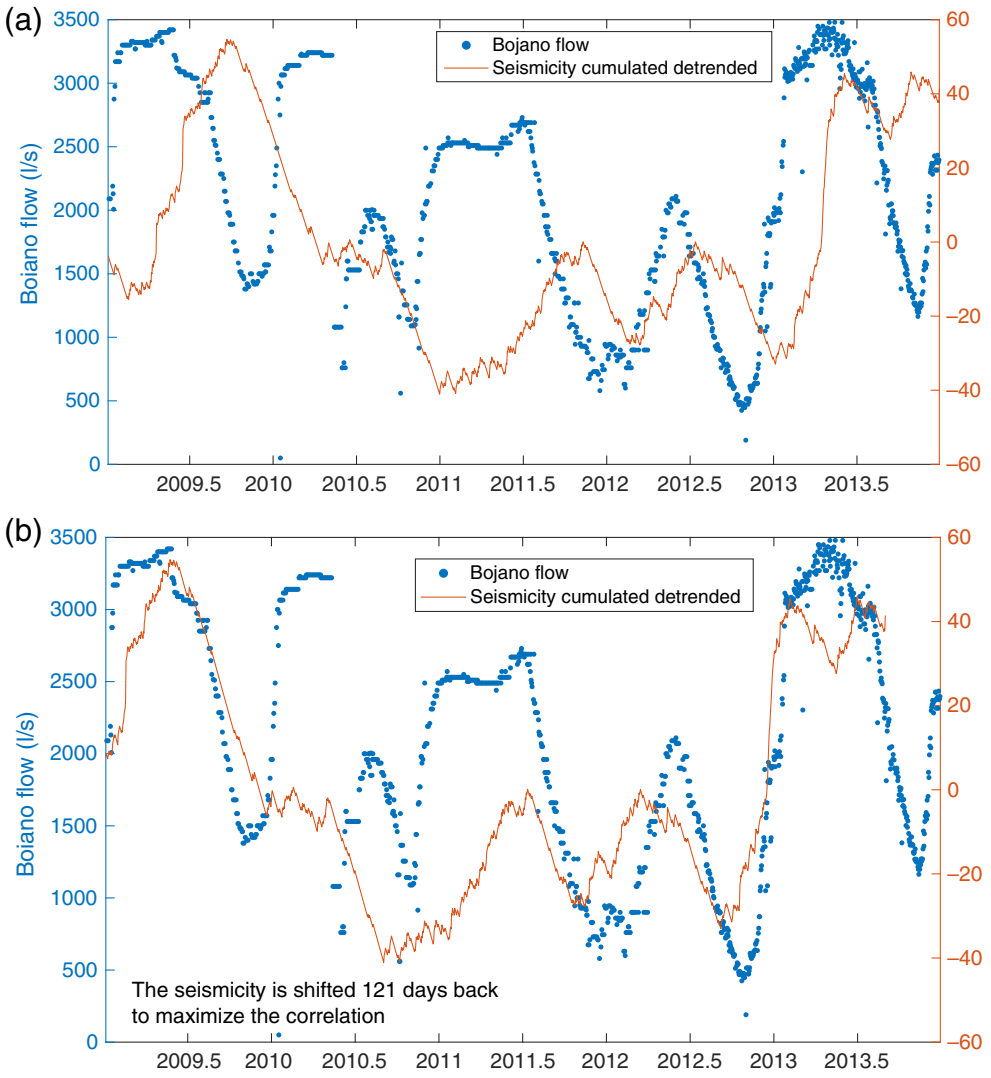

Figure 8. (a) Time series of Bojano spring discharge (blue) and seismicity (orange) from 2009 to 2013 and (b) the maximum correlation between time series is obtained when seismicity is shifted back by 121 days. The color version of this figure is available only in the electronic edition.

cannot exclude other nontectonic processes playing a role in activating the Matese seismicity, as for example magma intrusions (Di Luccio *et al.*, 2018).

Data and Resources

The seismic catalog was kindly provided by G. Diaferia and L. Valoroso just before its publication, it is now available at doi: 10.5281/zenodo.10054754 (Diaferia, 2023). The Global Navigation Satellite Systems (GNSS) data of the stations VAGA, LNGN, and PTRJ used in this study come from the RING network (http://ring.gm.ingv.it/), the station VINC is a part of the NETGEO Global Navigation Satellite Systems/Global Positioning System (GNSS/GPS) network (http://www.netgeo.it/page.php?Id=62), the ALIF station belongs to the Campania Regional GNSS/GPS network (http://gps.sit.regione.campania.it/indexmain.php), and the SGDS station to the HEXAGON network (https://hexagon.com/products/hxgn-smartnet). Spring discharge daily observations are provided by Regione Campania (http://centrofunzionale.regione.campania.it/#/pages/dashboard). The displacements caused by the effect of the hydrological and of the atmospheric loading are estimated using the products of the GeoForschungsZentrum (GFZ) downloaded from http://rz-vm115.gfz-potsdam.de:8080/repository/entry/show?entryid=24aacdfe-f9b0-43b7-b4c4-bdbe51b6671b (last accessed July 2023). Most of the figures were made using the Generic Mapping Tools (GMT) software (Wessel *et al.*, 2013). We used the Comsol Multiphysics software (https://www.comsol.com/) to model the displacements caused by the fracture opening. The principal component analysis (PCA) is performed using the vbICA code (Gualandi and Pintori, 2020) (https://data.mendeley.com/datasets/n92vwbg8zt/1). The information about the Istituto Nazionale di Geofisica e Vulcanologia (INGV) is available at http://terremoti.ingv.it/event/2874261. All websites were last accessed in July 2023. Finally, some additional figures are presented in the supplemental material.

Declaration of Competing Interests

The authors acknowledge that there are no conflicts of interest recorded.

Acknowledgments

The authors are grateful to Nicola D'Agostino and an anonymous reviewer; their suggestions helped them to improve the article. The authors wish to acknowledge Regione Campania, who have provided spring discharge data. The authors are grateful to A. Borghi, R. Devoti, and L. Faenza for the fruitful discussions. The authors acknowledge E. Serpelloni for the use of the Comsol Multiphysics software. This work got inspired from FURTHER, Earthquake Department Strategic Project "The role of FlUids in the pReparaTory pHase of EaRthquakes in Southern Apennines" of the Istituto Nazionale di Geofisica e Vulcanologia (INGV).

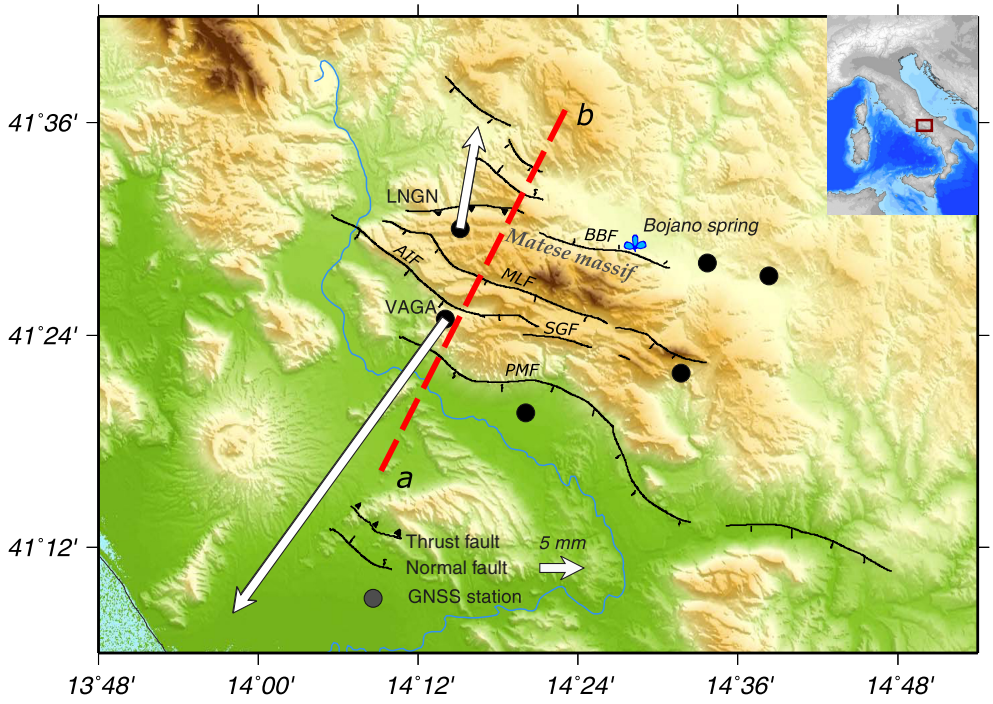

Figure 9. Map of the study area. The white arrows represent the maximum horizontal displacement associated with PC1. The red dashed line represents the orientation of the profile along which the finite-element method (FEM) model is built. The inset represents the study area and its location with respect to the Italian peninsula. The color version of this figure is available only in the electronic edition.

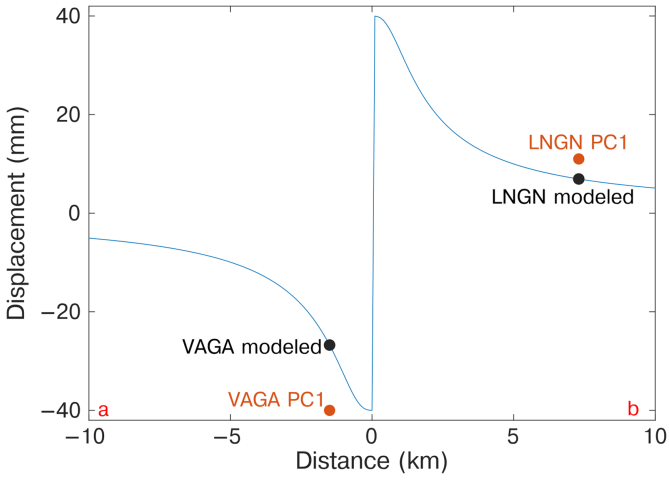

Figure 10. Comparison between the FEM-modeled displacements (black dots) and the displacements reconstructed by PC1 (orange dots) along the profile shown in Figure 9. The red letters (a) and (b) indicates the south-west and the north-east edge of the profile, as in Figure 9. The blue line represents the displacement field of the FEM model, where the fracture is located at distance = 0. Positive and negative displacements values indicate displacements toward north-east and south-west, respectively. The color version of this figure is available only in the electronic edition.

References

Beutler, G., H. Bock, R. Dach, P. Fridez, A. Gäde, U. Hugentobler, A. Jäggi, M. Meindl, L. Mervart, L. Prange, *et al.* (2007). Bernese GPS Software Version 5.0, in R. Dach, U. Hugentobler, P. Fridez, and M. Meindl (Editors), Astronomical Institute, University of Bern.

Bollinger, L., F. Perrier, J. P. Avouac, S. Sapkota, U. Gautam, and D. R. Tiwari (2007). Seasonal modulation of seismicity in the Himalaya of Nepal, *Geophys. Res. Lett.* **34,** no. 8, L08304, doi: 10.1029/2006GL029192.

Boncio, P., E. Auciello, V. Amato, P. Aucelli, P. Petrosino, A. C. Tangari, and B. R. Jicha (2022). Late Quaternary faulting in the southern Matese (Italy): Implications for earthquake potential and slip rate variability in the southern Apennines, *Solid Earth* **13,** 553–582, doi: 10.5194/se-13-553-2022.

Celico, F., E. Petrella, and P. Celico (2006). Hydrogeological behaviour of some fault zones in a carbonate aquifer of Southern Italy: An experimentally based model, *Terra Nova* **18,** 308–313, doi: 10.1111/j.1365-3121.2006.00694.x.

Craig, T. J., K. Chanard, and E. Calais (2017). Hydrologically-driven crustal stresses and seismicity in the New Madrid Seismic Zone, *Nat. Commun.* **8,** 2143, doi: 10.1038/s41467-017-01696-w.

D'Agostino, N., F. Silverii, O. Amoroso, V. Convertito, F. Fiorillo, G. Ventafridda, and A. Zollo (2018). Crustal deformation and seismicity modulated by groundwater recharge of karst aquifers, *Geophys. Res. Lett.* **45,** no. 22, 12–253, doi: 10.1029/2018GL079794.

Devoti, R., N. D'Agostino, E. Serpelloni, G. Pietrantonio, F. Riguzzi, A. Avallone, A. Cavaliere, D. Cheloni, G. Cecere, C. D'Ambrosio, *et al.* (2017). A combined velocity field of the Mediterranean region, *Ann. Geophys.* **60,** S0215, doi: 10.4401/ag-7059.

Devoti, R., F. Riguzzi, F. R. Cinti, and G. Ventura (2018). Long-term strain oscillations related to the hydrological interaction between aquifers in intra-mountain basins: A case study from Apennines Chain (Italy), *Earth Planet. Sci. Lett.* **501,** 1–12, doi: 10.1016/j.epsl.2018.08.014.

Devoti, R., D. Zuliani, C. Braitenberg, P. Fabris, and B. Grillo (2015). Hydrologically induced slope deformations detected by GPS and clinometric surveys in the Cansiglio Plateau, Southern Alps, *Earth Planet. Sci. Lett.* **419,** 134–142, doi: 10.1016/j.epsl.2015.03.023.

Diaferia, G. (2023). High-resolution earthquake catalog obtained through template-matching in the Southern Apennine (Italy) [Data set], *Zenodo*, doi: 10.5281/zenodo.10054754.

Diaferia, G., L. Valoroso, D. Piccinini, and L. Improta (2023). A new high resolution earthquake catalog for the Southern Apennines (Italy) built through template-matching, *Geochem. Geophys. Geosys.* doi: 10.22541/essoar.169111378.88427772/v1.

Dill, R. (2008). Hydrological model LSDM for operational earth rotation and gravity field variations, *Deutsches GeoForschungsZentrum GFZ* [Data Set], doi: 10.2312/gfz.b103-08095.

Dill, R., and H. Dobslaw (2013). Numerical simulations of global-scale high-resolution hydrological crustal deformations, *J. Geophys. Res.* **118,** 5008–5017, doi: 10.1002/jgrb.50353.

Di Luccio, F., G. Chiodini, S. Caliro, C. Cardellini, V. Convertito, N. A. Pino, C. Tolomei, and G. Ventura (2018). Seismic signature of active intrusions in mountain chains, *Sci. Adv.* **4,** e1701825, doi: 10.1126/sciadv.1701825.

Di Luccio, F., G. Ventura, R. Di Giovambattista, A. Piscini, and F. R. Cinti (2010). Normal faults and thrusts reactivated by deep fluids: The 6 April 2009 Mw 6.3 L'Aquila earthquake, central Italy, *J. Geophys. Res.* **115,** no. B6, doi: 10.1029/2009JB007190.

Dong, D., P. Fang, Y. Bock, M. Cheng, and S. Miyazaki (2002). Anatomy of apparent seasonal variations from GPS-derived site position time series, *J. Geophys. Res.* **107,** no. B4, 2075, doi: 10.1029/2001JB000573.

Esposito, A., A. Galvani, V. Sepe, S. Atzori, G. Brandi, E. Cubellis, P. De Martino, M. Dolce, A. Massucci, F. Obrizzo, *et al.* (2020). Concurrent deformation processes in the Matese massif area (Central-Southern Apennines, Italy), *Tectonophysics* **774,** 228–234, doi: 10.1016/j.tecto.2019.228234.

Ferrarini, F., P. Boncio, R. de Nardis, G. Pappone, M. Cesarano, P. P. C. Aucelli, and G. Lavecchia (2017). Segmentation pattern and structural complexities in seismogenic extensional settings: The North Matese Fault System (Central Italy), *J. Struct. Geol.* **95,** 93–112, doi: 10.1016/j.jsg.2016.11.006.

Fiorillo, F., and M. Pagnozzi (2015). Recharge process of Matese karst massif (southern Italy), *Environ. Earth. Sci.* **74,** 7557–7570, doi: 10.1007/s12665-015-4678-y.

Gardner, J. K., and L. Knopoff (1974). Is the sequence of earthquakes in Southern California, with aftershocks removed, Poissonian? *Bull. Seismol. Soc. Am.* **64,** no. 5, 1363–1367.

Gualandi, A., and F. Pintori (2020). "vbICA code", Mendeley Data, V1, doi: 10.17632/n92vwbg8zt.1

Gualandi, A., E. Serpelloni, and M. E. Belardinelli (2014). Space-time evolution of crustal deformation related to the M w 6.3, 2009 L'Aquila earthquake (central Italy) from principal component analysis inversion of GPS position time-series, *Geophys. J. Int.* **197,** no. 1, 174–191, doi: 10.1093/gji/ggt522.

Gualandi, A., E. Serpelloni, and M. E. Belardinelli (2016), Blind source separation problem in GPS time series, *J. Geodesy* **90,** no. 4, 323–341, doi: 10.1007/s00190-015-0875-4.

Gudmundsson, A. (1999). Fluid overpressure and stress drop in fault zones, *Geophys. Res. Lett.* **26,** 115–118, doi: 10.1029/1998GL900228.

Hainzl, S., T. Kraft, J. Wassermann, H. Igel, and E. Schmedes (2006). Evidence for rainfall-triggered earthquake activity, *Geophys. Res. Lett.* **33,** L19303, doi: 10.1029/2006GL027642.

Hsu, Y.-J., H. Kao, R. Bürgmann, Y.-T. Lee, H.-H. Huang, Y.-F. Hsu, Y.-M. Wu, and J. Zhuang (2021). Synchronized and asynchronous modulation of seismicity by hydrological loading: A case study in Taiwan, *Sci. Adv.* **7,** eabf7282, doi: 10.1126/sciadv.abf7282.

Iscan, A. G., M. V. Kök, and A. S. Bagcı (2006). Estimation of permeability and rock mechanical properties of limestone reservoir rocks under stress conditions by strain gauge, *J. Petrol. Sci. Eng.* **53,** 13–24, doi: 10.1016/j.petrol.2006.01.008.

Johnson, C. W., Y. Fu, and R. Bürgmann (2020). Hydrospheric modulation of stress and seismicity on shallow faults in southern Alaska, *Earth Planet. Sci. Lett.* **530,** 115904, doi: 10.1016/j.epsl.2019.115904.

Jolliffe, I. T. (2002). *Principal Component Analysis For Special Types of Data*, Springer, New York, New York.

Kositsky, A. P., and J. P. Avouac (2010). Inverting geodetic time series with a principal component analysis-based inversion method, *J. Geophys. Res.* **115,** no. B3, B03401, doi: 10.1029/2009JB006535.

Leone, G., N. D'Agostino, L. Esposito, and F. Fiorillo (2023). Hydrological deformation of karst aquifers detected by GPS measurements, Matese massif, Italy, *Environ. Earth Sci.* **82,** 240, doi: 10.1007/s12665-023-10905-3.

Madhubabu, N., P. K. Singh, A. Kainthola, B. Mahanta, A. Tripathy, and T. N. Singh (2016). Prediction of compressive strength and elastic modulus of carbonate rocks, *Measurement* **88,** 202–213, doi: 10.1016/j.measurement.2016.03.050.

Miller, S. A., C. Collettini, L. Chiaraluce, M. Cocco, M. Barchi, and B. J. P. Kaus (2004). Aftershocks driven by a high-pressure CO_2 source at depth, *Nature* **427,** 724–727, doi: 10.1038/nature02251.

Montgomery-Brown, E. K., D. R. Shelly, and P. A. Hsieh (2019). Snowmelt-triggered earthquake swarms at the margin of Long Valley Caldera, California, *Geophys. Res. Lett.* **46,** 3698–3705, doi: 10.1029/2019GL082254.

Nespoli, M., N. Cenni, M. E. Belardinelli, and M. Marcaccio (2021). The interaction between displacements and water level changes due to natural and anthropogenic effects in the Po Plain (Italy): The different point of view of GNSS and piezometers, *J. Hydrol.* **596,** 126112, doi: 10.1016/j.jhydrol.2021.126112.

Patacca, E., and P. Scandone (2007). Geology of the southern Apennines, *Boll. Soc. Geol. Ital.* **7,** 75–119.

Petrella, E., D. Aquino, F. Fiorillo, and F. Celico (2015). The effect of low-permeability fault zones on groundwater flow in a compartmentalized system. Experimental evidence from a carbonate aquifer (Southern Italy), *Hydrol. Processes* **29,** no. 6, 1577–1587, doi: 10.1002/hyp.10294.

Pintori, F., E. Serpelloni, and A. Gualandi (2022). Common mode signals and vertical velocities in the great Alpine area from GNSS data, *Solid Earth Discuss.* **13,** 1541–1567, doi: 10.5194/se-13-1541-2022.

Pintori, F., E. Serpelloni, L. Longuevergne, A. Garcia, L. Faenza, L. D'Alberto, A. Gualandi, and M. E. Belardinelli (2021). Mechanical response of shallow crust to groundwater storage variations: Inferences from deformation and seismic observations in the Eastern Southern Alps, Italy, *J. Geophys. Res.* **126,** no. 2, e2020JB020586, doi: 10.1029/2020JB020586.

Rice, J. R., and M. P. Cleary (1976). Some basic stress diffusion solutions for fluid-saturated elastic porous media with compressible constituents, *Rev. Geophys.* **14,** no. 2, 227–241, doi: 10.1029/RG014i002p00227.

Roeloffs, E. A. (1988). Fault stability changes induced beneath a reservoir with cyclic variations in water level, *J. Geophys. Res.* **93,** no. B3, 2107–2124, doi: 10.1029/JB093iB03p02107.

Rovida, A., M. Locati, R. Camassi, B. Lolli, P. Gasperini, and A. Antonucci (2022). Catalogo Parametrico dei Terremoti Italiani

(CPTI15), Versione 4.0, Istituto Nazionale di Geofisica e Vulcanologia (INGV), doi: 10.13127/CPTI/CPTI15.4.

Schuite, J., L. Longuevergne, O. Bour, T. J. Burbey, F. Boudin, N. Lavenant, and P. Davy (2017). Understanding the hydromechanical behavior of a fault zone from transient surface tilt and fluid pressure observations at hourly time scales, *Water Resour. Res.* **53,** no. 12, 10,558–10,582, doi: 10.1002/2017WR020588.

Serpelloni, E., A. Cavaliere, L. Martelli, F. Pintori, L. Anderlini, A. Borghi, D. Randazzo, S. Bruni, R. Devoti, P. Perfetti, *et al.* (2022). Surface velocities and strain-rates in the Euro-Mediterranean region from massive GPS data processing, *Front. Earth Sci.* **10,** 907897, doi: 10.3389/feart.2022.907897.

Serpelloni, E., F. Pintori, A. Gualandi, E. Scoccimarro, A. Cavaliere, L. Anderlini, M. E. Belardinelli, and M. Todesco (2018). Hydrologically induced karst deformation: Insights from GPS measurements in the Adria-Eurasia plate boundary zone, *J. Geophys. Res.* **123,** 4413–4430, doi: 10.1002/2017JB015252.

Shapiro, S. A., R. Patzig, E. Rothert, and J. Rindschwentner (2003). Triggering of seismicity by pore-pressure perturbations: Permeability-related signatures of the phenomenon, *Pure Appl. Geophys.* **160,** 1051–1066, doi: 10.1007/PL00012560.

Sibson, R. H., and J. V. Rowland (2003). Stress, fluid pressure and structural permeability in seismogenic crust, North Island, New Zealand, *Geophys. J. Int.* **154,** no. 2, 584–594, doi: 10.1046/j.1365-246X.2003.01965.x.

Silverii, F., N. D'Agostino, A. Borsa, S. Calcaterra, P. Gambino, R. Giuliani, and M. Mattone (2019). Transient crustal deformation from karst aquifers hydrology in the Apennines (Italy), *Earth Planet. Sci. Lett.* **506,** 23–33, doi: 10.1016/j.epsl.2018.10.019.

Silverii, F., N. D'Agostino, M. Métois, F. Fiorillo, and G. Ventafridda (2016). Transient deformation of karst aquifers due to seasonal and multiyear groundwater variations observed by GPS in southern Apennines (Italy), *J. Geophys. Res.* **121,** no. 11, 8315–8337, doi: 10.1002/2016JB013361.

Talwani, P. (1997). On the nature of reservoir-induced seismicity, *Pure Appl. Geophys.* **150,** 473–492, doi: 10.1007/s000240050089.

Talwani, P., L. Chen, and K. Gahalaut (2007). Seismogenic permeability, k_s, *J. Geophys. Res.* **112,** B07309, doi: 10.1029/2006JB004665.

Taroni, M., and A. Akinci (2021). Good practices in PSHA: Declustering, b-value estimation, foreshocks and aftershocks inclusion; a case study in Italy, *Geophys. J. Int.* **224,** no. 2, 1174–1187, doi: 10.1093/gji/ggaa462.

Wells, D. L., and K. J. Coppersmith (1994). New empirical relationships among magnitude, rupture length, rupture width, rupture area, and surface displacement, *Bull. Seismol. Soc. Am.* **84,** no. 4, 974–1002, doi: 10.1785/BSSA0840040974.

Wessel, P., W. H. F. Smith, R. Scharroo, J. F. Luis, and F. Wobbe (2013). Generic mapping tools: Improved version released, *Eos Trans. AGU* **94,** no. 45, 409–410, doi: 10.1002/2013EO450001.

Wiemer, S. (2001). A software package to analyze seismicity: ZMAP, *Seismol. Res. Lett.* **72,** no. 3, 373–382, doi: 10.1785/gssrl.72.3.373.

Manuscript received 20 July 2023
Published online 27 December 2023